

Backscattering Behavior of Vulnerable Road Users Based on High-Resolution RCS Measurements

Sevda Abadpour¹, Member, IEEE, Sören Marahrens², Mario Pauli³, Senior Member, IEEE, Jan Siska, Member, IEEE, Nils Pohl⁴, Senior Member, IEEE, and Thomas Zwick⁵, Fellow, IEEE

Abstract—Automotive radars, along with optical sensors such as cameras or lidars, offer a reliable way of obtaining the 3-D information about the environment. Of particular interest in autonomous driving (AD) is the reliable detection of particularly vulnerable road users (VRUs). Modern radar sensors are able to detect, distinguish, and track targets with high resolution. Relying on that, a backscattering model of complex traffic targets can be generated from the reflected signals of their scattering points (SPs). These models can be employed in the radar channel simulations for verification methods of advanced driver assistance systems. Therefore, in this work, different persons as the most vital VRUs are measured with high radial and high angular resolution. The necessary signal processing steps are explained in detail for the determination of the relevant SPs. Thus, the corresponding radar cross section (RCS) values can be assigned to certain body regions. In addition to real persons, further measurements are compared with a dummy of the corresponding size. Based on the measurement results, not only accurate models of road users can be derived, but also the measurement results can be employed for calculating wave propagation in traffic scenarios. From the measured SPs, the classification of the persons by size and stature is derived.

Index Terms—Human body radar cross section (RCS) measurement, radar high-resolution measurement, RCS modeling of extended targets, scattering points (SPs), traffic objects, vulnerable road users (VRUs).

I. INTRODUCTION

THE safety of vulnerable road users (VRUs) is of utmost importance in the field of autonomous driving (AD). The advanced driver assistance system (ADAS) is a set of intelligent solutions incorporated into AD systems to increase

the safety of self-driving vehicles [1]. Any fault in this system may lead to hazardous situations and even fatal accidents. The newest generation of microwave sensors, as the core of ADAS [2], can be the game-changer technology and make it easier to avoid accidents, casualties, and losses involved. Different objects, e.g., motorcyclists, cyclists, users of electric scooters, and, in particular, pedestrians, are a subset of VRUs. Most of the VRUs, especially pedestrians and cyclists, have a variety of movement options and their behavior in the traffic scenes is agile. Therefore, modeling their motion in traffic scenarios is essential to, on one hand, identify them in a timely manner and, on the other hand, foresee dangerous situations [1], [3]. Automotive radars are the first-rate nominees for this task since, unlike cameras, they remain robust in adverse weather conditions to measure the range, radial velocity, and angle of the objects.

ADAS has a safety-critical nature, and thereby, it is crucial to ensure the stable, reliable, and safe functionality of ADAS for every conceivable driving situation before the system can go into operation. It demands test approaches with sufficient degrees of realism, affordable cost, and reproducible and controllable conditions on software and hardware under all contingencies. The necessary prerequisites for approaching the full automation level in self-driving cars are software-in-the-loop (SiL), hardware-in-the-loop (HiL) simulations, and over-the-air (OTA) vehicle-in-the-loop (ViL) emulation before the on-road testing [4].

Testing the systems in the field might offer a high degree of realism; however, it offers a potential risk to other traffic participants and involves an enormous effort. As discussed elsewhere [5], [6], several million kilometers of test drives are necessary to ensure the correct functioning at a safety level higher than a human driver. Another disadvantage of driving in the field is that the conditions are not repeatable since most of the traffic situations are constantly changing and the same situation on the field can hardly be reproduced after changing the automotive sensor configuration and software. On the other hand, the mentioned validation methods, SiL, HiL, and/or OTA-ViL, enable researchers and engineers to simulate different traffic situations, especially critical ones, in laboratory conditions instead of field tests. The OTA-ViL method offers resilient and reliable testing and evaluation of real operational radar systems with providing a complete picture of the vehicle's surroundings and its ability to recognize the environment. By using a dedicated radar target simulation

Manuscript received September 8, 2021; revised October 23, 2021; accepted October 24, 2021. This work was supported in part by the German Federal Ministry of Education and Research (BMBF) through the VIVID Project under Grant 16ME0171 and in part by the German Research Foundation (Deutsche Forschungsgemeinschaft (DFG), for Project C03) under Project-ID 287022738 TRR 196. (Corresponding author: Sevda Abadpour.)

This work involved human subjects or animals in its research. Approval of all ethical and experimental procedures and protocols was granted by the KIT Ethics Committee.

Sevda Abadpour, Mario Pauli, and Thomas Zwick are with the Institute of Radio Frequency Engineering and Electronics (IHE), Karlsruhe Institute of Technology (KIT), 76131 Karlsruhe, Germany (e-mail: sevda.abadpour@kit.edu).

Sören Marahrens is with Nemko GmbH & Co. KG, 76327 Pfinztal, Germany.

Jan Siska and Nils Pohl are with the Institute for Integrated Systems, Ruhr University Bochum, 44801 Bochum, Germany.

Color versions of one or more figures in this article are available at <https://doi.org/10.1109/TMTT.2021.3131156>.

Digital Object Identifier 10.1109/TMTT.2021.3131156

system [7] that is capable to generate multiple radial and angle-resolved targets, the emulation of standard and complex environments can be performed authentically. However, an essential prerequisite for a realistic target simulation is the knowledge of the distribution of the scattering points (SPs) of the real target (e.g., car, motorcycle, and VRUs) that has to be represented by the radar target simulator. Only in this case, the radar wave propagation behavior is similar to the real environment and the sensor response can be compared.

The automotive radar sensors are sensing the surrounding environment based on the detection points determined by studying their backscattering behavior. Modern automotive radars are capable of sensing multiple reflections from real-life targets and deliver a rich set of measurement data. In this way, radars can resolve multiple SPs of an object. Accordingly, reflected signals from numerous SPs of various traffic participants can be utilized to generate radar targets in the radar target simulator and subsequently simulate the backscattering behavior of real traffic scenarios [8]. Thus, developing a precise model of the traffic participants, especially VRUs, which includes their backscattering behavior, is a challenge and gained high interest in research and development. The implementation of the scattering process into the radar wave propagation simulation can be done in different ways as explained in [8]–[15] in detail and summarized in [8]. High-resolution radar cross section (RCS) measurements in the radial and the angular domain can be used for backscattering models in the wave propagation simulations and thus speed up simulations. Furthermore, due to their unique accuracy, these models give new insights to the radar-specific characteristics of VRUs and can be used in the next step to greatly improve micro-Doppler models of traffic participants and thus lead to better classifications. Besides, the extracted radar models can be utilized for target classification based on millimeter-wave (mm-wave) radar data. There are different radar target classification methods for the traditional and modern radars (with imaging capability) in the literature [16]–[18]. The approaches follow different types of radar data, such as distributed RCS data classification for traditional range-detection radar, Doppler signature analysis, 2-D range-azimuth angle radar images classification for radars capable of scanning in the azimuth direction, and 3-D radar images for radars with both azimuth and elevation direction beam-scanning ability. Moreover, the radar image-based target classification can provide the greatest potential for target classification [16].

Despite improvements in the protection of car passengers due to the steady progress of safety functions in the last decades, the protection of VRUs, especially pedestrians, still remains a crucial issue [19]. Accordingly, this work aims to close the gap between vehicle and VRUs safety by offering high-resolution radar models. The literature already contains several reports presenting the RCS patterns of pedestrian [9], [20], [21]. However, these patterns are often very abstract and show only an integral value of the complete object but not a detailed distribution of the SPs over the surface of the object. Hence, these models can rarely be used for precise simulations of the radar channel. Moreover, it is of evident interest to investigate whether the RCS pattern and the distribution of

the SPs along the body of a dummy human are comparable to that of a real human. Only in this case, dangerous traffic maneuvers can be tested in the field and compared to ViL simulations [22]. Addressing those issues, the purpose of this article is to propose and investigate radar models of VRUs based on high-resolution RCS measurements for humans with different sizes and a comparable dummy human.

In this context, Section II discusses the measurement setup based on a frequency-modulated continuous-wave (FMCW) radar sensor for high-resolution monostatic RCS measurements. First, well-known standard targets are measured to extract the radar two-way radiation characteristics. Only if the radiation pattern of the own Radar system is known, the results of the subsequent RCS measurements can be interpreted correctly. Subsequently, the RCS measurement setup is discussed, and the process of extraction of the SPs for different sized persons is described. Accordingly, dedicated measurements are arranged to scan the volunteer persons and dummy human in different view angles. Results of different human objects are analyzed in Section III. Section III presents an algorithm to approximate the surface contour and extract the radar model of the VRU under study. This section continues with predicting the location of human body parts and estimating the detailed sizes of the measured models. In addition, this section compares the measurement results of a human dummy with a person having comparable sizes. The last part of Section III-B briefly discusses target classification based on the extracted radar models from the measurement. Finally, this work is concluded in Section IV.

II. MEASUREMENT SETUP

A. High-Resolution mm-Wave Radar Sensor

Today's SiGe semiconductor technology allows for the integration of complex ultrawideband radar transceivers in the mm-wave band for the highest resolution at moderate costs. This enables extremely precise distance and movement determination.

This work exploits a radar sensor, developed by Ruhr-Universität Bochum (RUB) and fabricated using Infineon's B7HF200 SiGe automotive production technology [23], [24]. The sensor is an FMCW radar, based on an ultrawideband oscillator, synthesizer, and receiver with 25-GHz bandwidth around the center frequency of 80 GHz. The software of the sensor allows the user to adjust the working bandwidth and center frequency within the given range [23]. The configured bandwidth and center frequency of the radar in this work are 5 GHz and 78.5 GHz, to comply with the equivalent automotive radar bands. This enables high-resolution radar measurements with a radial resolution of 3 cm. The complete radar sensor is packaged into a metallic housing with a single micro-USB interface for power and data [23].

For the RCS measurements in this work, a horn antenna with 20-dBi gain is mounted on the top of the radar. The radar sensor is mounted on a two-axis motorized turn-tilt table to provide the mechanical scanning capability. The turn-tilt table is embedded in the radar control unit (RCU) to rotate the radar sensor in both azimuth and elevation directions with

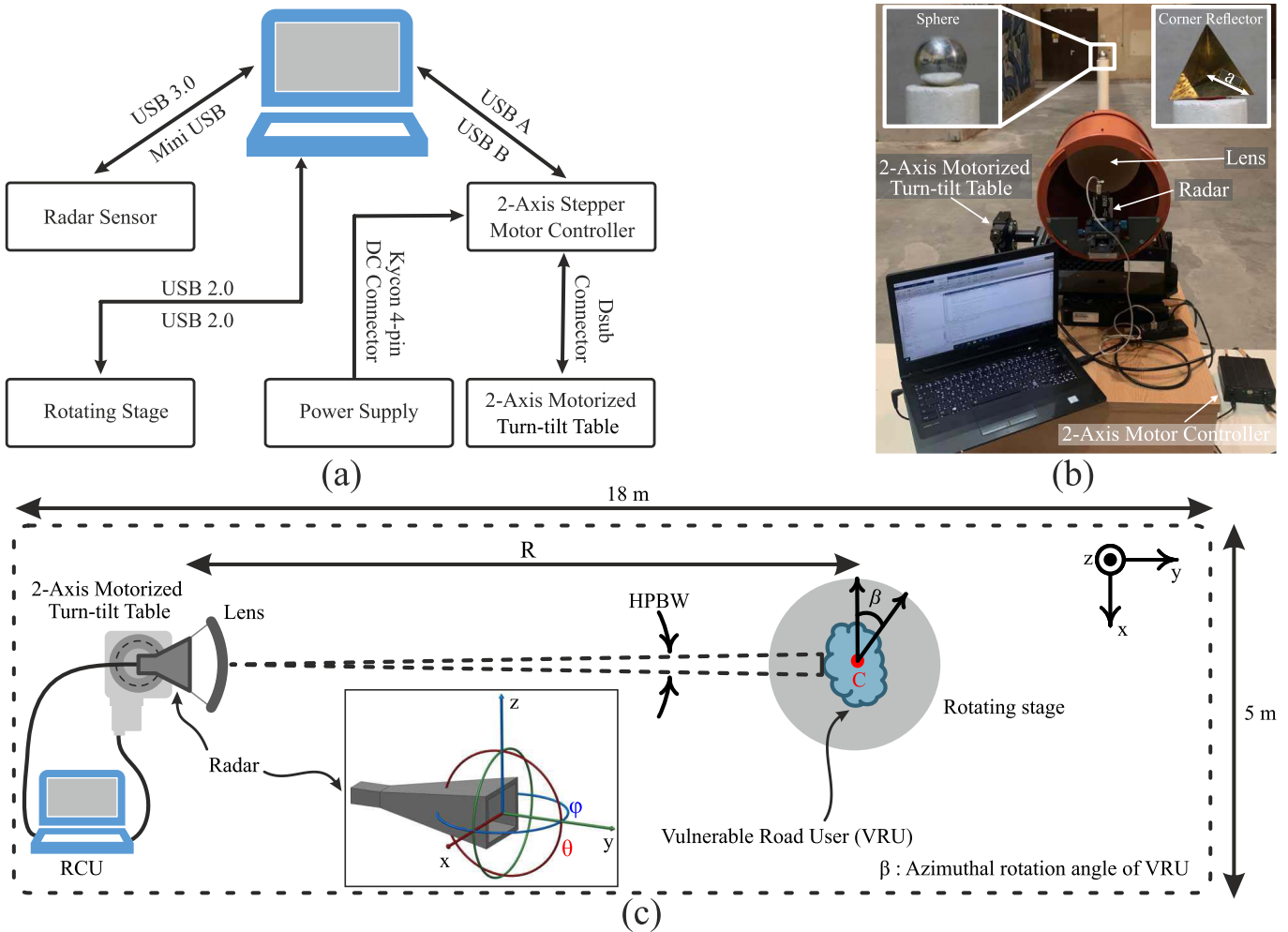


Fig. 1. (a) Block diagram of the RCU. (b) Setup for measuring the two-way radiation pattern of the Radar system using a sphere as a standard object. (c) Block diagram of measurement setup to detect the SPs of VRU with its azimuthal rotation angle (β) for radar model extraction. The rotation angles of the radar in azimuth (ϕ) and elevation (θ) directions as well as the radar coordinate system are shown in the inset.

the desired angular resolution. The schematic of the setup of the RCU is shown in Fig. 1(a). This system consists of the mm-wave FMCW radar sensor, a laptop, a two-axis stepper motor controller, a two-axis motorized turn-tilt table, and a power supply. Before starting the measurement procedure, the turn-tilt table and sensor are initialized by the laptop via USB interfaces. During the measurement, the laptop controls the turn-tilt table to collect the angular-dependent raw data of the radar sensor. The two-way radiation pattern of the radar with the horn antenna is measured using a metallic sphere with a radius of 17.8 cm as a calibration target. The measurement of the two-way radiation pattern is performed within an anechoic chamber in the Institute of Radio Frequency Engineering and Electronics (IHE), KIT. The sphere is placed at a distance of 4.7 m to the radar. The measured half-power beamwidth (HPBW) of the radar sensor using the 20-dBi horn antenna is 18° . Considering the 3-cm radial resolution of the radar, its range resolution is sufficient for the high-resolution measurement. However, the HPBW of 18° is not appropriate for detailed scattering models of complex traffic objects. In a measurement distance of 9 m, the VRU is illuminated as a whole by the radar, resulting in an integral

RCS pattern without the ability to distinguish between multiple reflection points in angular directions. To focus the main beam, a dielectric polytetrafluoroethylene (PTFE) lens is designed and mounted to the radar sensor, as shown in Fig. 1(b) and (c). The PTFE lens antenna has a diameter of 205 mm and focuses the radar to an HPBW of 1.3° and a gain of 40.5 dBi.

The radar together with the corresponding high-focusing PTFE lens antenna will be called the ‘‘Radar system’’ throughout this work. Section II-B discusses the specification of the Radar system in more detail.

B. Extracting the Two-Way Radiation Pattern of the Radar System

The two-way radiation pattern of the Radar system is measured to evaluate the HPBW and the first sidelobe level (SLL) of the sensor with the lens. In addition, it is beneficial to analyze the reflection angle of the incident waves. The measurement is conducted in a large hall, provided by the Institute for Pulsed Power and Microwave Technology (IHM), KIT. A section of the hall with the dimension of $18\text{ m} \times 5\text{ m} \times 30\text{ m}$

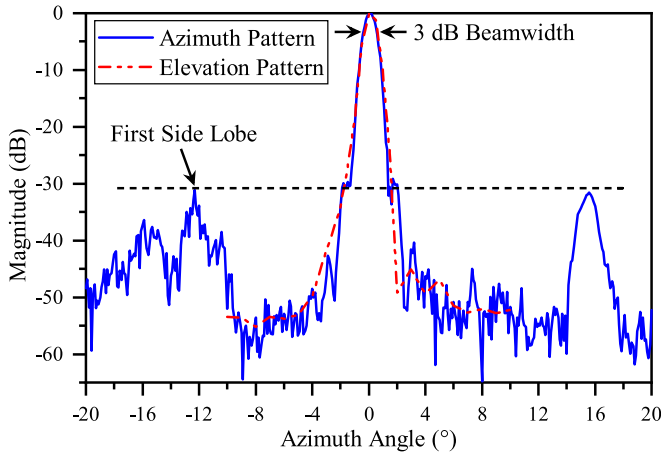


Fig. 2. Measured two-way radiation pattern of the radar equipped with the lens antenna in azimuth and elevation directions.

($L \times W \times H$) is selected for the radar test setup and the monostatic RCS measurements.

Fig. 1(c) shows the schematic of the measurement setup. The phase center of the feeding horn antenna of the Radar system is positioned in one of the ellipsoidal focal points of the lens. The distance between the center of the object under test (C) and the feed antenna is denoted as R . As shown in Fig. 1(c), the motorized turn-tilt table enables the Radar system to scan the environment in both azimuth (ϕ) and elevation (θ) directions [inset Fig. 1(c), showing the coordinate system of the radar sensor]. The azimuth angle (ϕ) is the angle in the xy plane around the z -axis, where $\phi = 0^\circ$ points in direction of the y -axis. The elevation angle is defined as the angle in the yz plane around the x -axis, where $\theta = 0^\circ$ is defined in direction of the y -axis. The origin of the coordinate system is the phase center of the feeding horn antenna of the Radar system. The RCU controls the measurement and collects the raw data of the radar sensor.

Fig. 1(b) shows the details of the measurement setup in the test environment. For extracting the two-way radiation pattern of the Radar system, a standard sphere with a radius of 9 cm is positioned at the range of $R = 9$ m in the test setup. The sphere under test is placed on a Rohacell stand with a permittivity of $\epsilon_r \approx 1$ to avoid unwanted reflections. The center of the sphere is aligned to the main beam of the Radar system and is defined as the azimuth angle of 0° and the elevation angle of 0° . The scanning area for the two-way pattern measurement is set to $\pm 20^\circ$ in azimuth and $\pm 10^\circ$ in elevation to cover the size of all measured objects under test in this article.

The pencil-beam pattern of the Radar system in the azimuth and elevation directions is shown in Fig. 2. The patterns in elevation and azimuth directions are almost the same because of the rotational symmetry of the lens. According to the depicted patterns, the HPBW of the Radar system is 1.3° in both directions. The first SLL is -31.2 dB in the azimuth direction. The distortions at the left side of the radiation pattern in the azimuth direction (negative azimuth angles) are caused by the metallic equipment in the test environment, which could not be removed.

TABLE I
RADAR SYSTEM TECHNICAL SPECIFICATION

Parameter	Radar system Specification
Center Frequency (f_0)	78.5 GHz
Bandwidth (Δf)	5 GHz
HPBW	1.3° in Azimuth and Elevation direction
Chirp Time (T_{sweep})	4 ms (saw tooth)
Antenna Gain (G)	40.5 dBi
Transmit Power (P_{Tx})	-6 dBm
Noise Figure (NF)	20 dB
Integration Time for both θ and ϕ	5 s
Integration Time for β	60 s

The Radar system has an overall gain of 40.5 dBi. The specifications of the Radar system are summarized in Table I. These specifications confirm that the proposed Radar system satisfies the prerequisites for high-resolution RCS measurements.

C. Extracting the SPs of the VRUs

Compared to the wavelength at the operating frequency of the Radar system, the VRUs are electrically large objects. Hence, the RCS values depend on the relative orientation of the sensor and the VRU (corresponding to β) since only a part of the VRU is illuminated by the HPBW of the Radar system. Therefore, in addition to Radar system scanning angles θ and ϕ , the radar measurements studying the backscattering behavior of VRU should be conducted for different rotation angles β of the object under test. It is worth emphasizing that in total, three scanning parameters have been considered in these measurements: θ , ϕ , and β . This comes closer to the real application of an automotive radar, where the VRU is illuminated under different viewing angles, e.g., stepping into the street from the sidewalk. In a different approach based on the inverse synthetic aperture radar (ISAR) technique, Pieraccini *et al.* [25] illuminated the target with the antenna boresight and rotated the target. This procedure also allows for an image under test, and however, the current work also accounts for illumination with slant incidence and is closer to the real-world application.

For measuring the high-resolution monostatic RCS of the object under test, it is placed in front of the Radar system on the rotating stage. Then, the object under test is rotated around the z -axis with a tunable azimuthal resolution angle ($\Delta\beta$). Further details are given in Section III-B. The Radar system is placed at approximately half height of the object under test and in its center. The scanning area of the Radar system in elevation (θ) and azimuth (ϕ) directions is calculated according to the size of the object under test and the range (R) with a step width $\Delta\theta$ and $\Delta\phi$. Section III-B discusses it in more detail. The block diagram of the measurement setup for extracting the high-resolution radar model of the VRUs is similar to the one shown in Fig. 1(c). Fig. 3 shows the



Fig. 3. Setup for monostatic RCS measurement of VRUs to extract their radar model (dummy human is placed on top of the rotating stage for extracting its SPs).

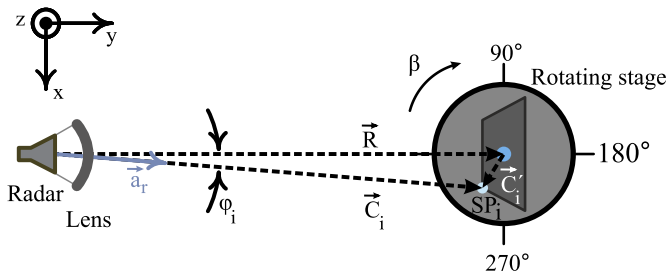


Fig. 4. Object under test where its front side is illuminated by the Radar system with a description of the relevant geometry and the coordinate system.

details of the measurement setup for different VRUs in the test environment.

In Fig. 3, the object under test is placed on the rotating stage at a distance of 9 m from the Radar system in order to collect the spatial distribution of the SPs of the VRU. The measurements are performed over the whole 360° azimuthal rotation angle. As a proof of concept, the reconstructed radar images corresponding to multiple rotation angles are shown in Section III-B.

III. MEASUREMENT RESULTS

A. Algorithm for Extracting the 3-D Extension of Targets From the Collected Data

As discussed in Section II, the measurement setup enables the collection of unprocessed raw data. These data correspond to the different values of θ , ϕ , and β and distance between the radar sensor and the center of the object under test (R). The 3-D reconstructions of the objects can be created to determine the location of different SPs on the body of VRUs precisely.

Fig. 4 shows the measurement setup with the coordinate systems and the relevant geometry to extract the SPs corresponding to each combination of the measurement parameters. The position of each scattering point (\vec{SP}_i) is obtained assuming the radar sensor as the origin of the spherical coordinate system ($\vec{C}_i = [C_i \ \phi_i \ \theta_i]$). For a certain azimuth angle of ϕ_i , elevation angle of θ_i , and \vec{R} (the vector connecting the sensor to the center of the object)

$$\vec{C}_i = \vec{R} + \vec{C}'_i \quad (1)$$

where \vec{C}'_i is the coordinate of SP_i , in the coordinate system whose origin is the center of the object. Therefore,

$$\vec{C}'_i = \|\vec{C}_i\| \vec{a}_r - R \vec{a}_y \quad (2)$$

where \vec{a}_y and \vec{a}_r are the unit vectors in the Cartesian and spherical coordinate systems, respectively. The sensor height influences the z component of \vec{C}'_i . In order to evaluate the 3-D RCS profile of the object, the standard rotation axis matrix can be expressed using the azimuthal rotation angle β as

$$\begin{bmatrix} x''_i \\ y''_i \\ z''_i \end{bmatrix} = \begin{bmatrix} \cos(\beta) & \sin(\beta) & 0 \\ -\sin(\beta) & \cos(\beta) & 0 \\ 0 & 0 & 1 \end{bmatrix} \begin{bmatrix} x'_i \\ y'_i \\ z'_i \end{bmatrix} \quad (3)$$

where x'_i , y'_i , and z'_i are the SP_i location in the radar coordinate system and x''_i , y''_i , and z''_i are the coordinates in the VRU coordinate system. These values can be used to generate the radar model of VRU. In other words

$$RCS_i = f(\phi_i, \theta_i, \beta_i). \quad (4)$$

The coordinates of the i th SP in the VRU Cartesian coordinate system can be written as

$$\vec{SP}_i = [x''_i \ y''_i \ z''_i]. \quad (5)$$

In the high-resolution monostatic RCS measurements, the RCS value of each extracted SP can be calculated from the received signal. The power received by the sensor (P_{Rx}) can be described by the radar equation for the monostatic case [26] as

$$P_{Rx} = \frac{P_{Tx} G^2 \lambda^2}{(4\pi)^3 R^4} RCS \quad (6)$$

where P_{Tx} is the transmit power of the sensor, G is the antenna gain of the monostatic radar, λ is the wavelength, and R is the distance between the radar sensor and the object under test. The received power can be calculated using the signal-to-noise ratio (SNR) of the Radar system

$$SNR = \frac{P_{Rx}}{P_N} \quad (7)$$

where P_N is the noise power at the receiver. P_N for an FMCW radar is

$$P_N = \frac{k T_{abs} NF}{T_{Sweep}} \quad (8)$$

where k is Boltzmann's constant, T_{abs} is the absolute temperature of the test environment, NF is the noise figure of the sensor, and T_{Sweep} is the chirp time. By comparing (6)–(8)

and the geometry in Fig. 4, the measured RCS value for the i th extracted SP (RCS_i) can be estimated by

$$RCS_i = \frac{(4\pi)^3 \|\vec{C}_i\|^4 k T_{\text{abs}} NF}{P_{\text{Tx}} G^2 T_{\text{Sweep}} \lambda^2} \text{SNR}_{\text{Meas},i} \quad (9)$$

where $\|\vec{C}_i\|$ is the radial distance between the radar sensor and the i th detected scattering point (SP $_i$) and $\text{SNR}_{\text{Meas},i}$ is the measured signal to the noise level for the i th SP. $\text{SNR}_{\text{Meas},i}$ can be calculated by

$$\text{SNR}_{\text{Meas},i} = \frac{S_{\text{Meas},i}}{N_{\text{Meas}}} \quad (10)$$

where $S_{\text{Meas},i}$ is the measured level of the signal in the place of the i th SP and N_{Meas} is the measured noise level of the Radar system when it is pointing toward the sky.

The high-resolution radar model can be constructed by employing the RCS values and their corresponding coordinates as

$$\text{SP} = \begin{bmatrix} x''_1 & y''_1 & z''_1 & RCS_1 \\ \vdots & \vdots & \vdots & \vdots \\ x''_i & y''_i & z''_i & RCS_i \\ \vdots & \vdots & \vdots & \vdots \\ x''_N & y''_N & z''_N & RCS_N \end{bmatrix} \quad (11)$$

where N is the total number of the extracted points.

To get normalized RCS values, a calibration of the measured RCS data is necessary. Therefore, in an additional calibration step, the RCS of a trihedral corner reflector (TCR) is measured and compared to its analytical value. The difference between these two values is subsequently used as a calibration factor. The analytical RCS of the TCR can be calculated [27] by

$$RCS = \frac{(4\pi)a^4}{3\lambda^2} \quad (12)$$

where a is the inner height of the TCR, as shown in Fig. 1(b), and λ is the wavelength. A TCR with the size of 4.4 cm is chosen for the calibration measurement in this work. Its analytical RCS value is determined 0.3 dBsm by using (12). The measured RCS value can be estimated from the measured reflected signal level in the measurement setup [Fig. 1(b)] and following (9) and (10). In this experiment, the TCR is positioned so that its center is aligned to the main beam of the Radar system. Considering the size of the TCR, the scanning range is set to $\pm 10^\circ$ in azimuth. Fig. 5 shows the measured RCS values. As shown in Fig. 5, the detected location of the TCR is at an azimuth angle of 0° and is within the HPBW area of the Radar system. Hence, the measured RCS is approximated 1.7 dBsm. Consequently, the calibration factor of the measurement setup is -1.4 dBsm.

As a secondary validation step and in order to be able to compare the results with the state of the art, a measurement on the human object is performed when the lens is removed. As the result, the object is considered as a single scattering point. Fig. 6 shows the measured RCS pattern for a human (with the height of 170 cm and shoulder width of 40 cm) object. The measured RCS values over the human azimuthal angle change between -16.6 and 0 dBsm, which are in good agreement with the reported values in [9] and [20].

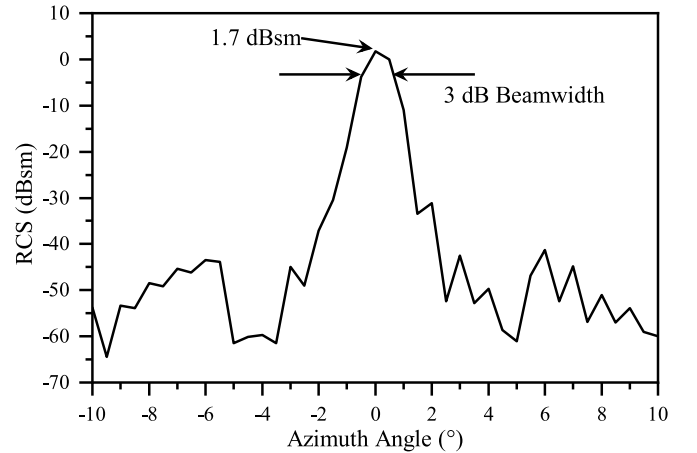


Fig. 5. Measured RCS value for a TCR with the size of 4.4 cm is positioned in the main beam of the Radar system in the azimuth scanning area of $\pm 10^\circ$. The TCR is detectable in 0° azimuth angle corresponding to the main beam of the Radar system.

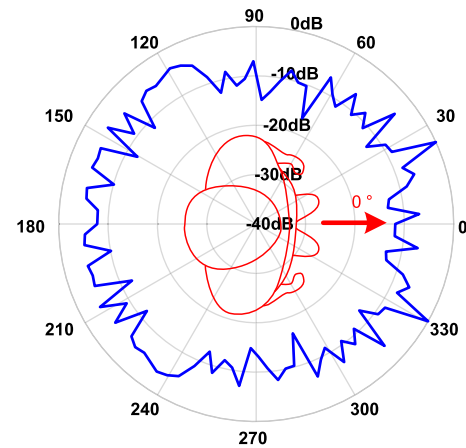


Fig. 6. Measured RCS pattern of a human at the measurement setup when the lens antenna is removed.

In another calibration step, the test environment is characterized. The signal, collected by the receiver antenna of the radar, comprises the signal reflected from the object under test, echoes from the unwanted objects in the test environment (also known as clutter), and thermal noise. Therefore, the environment clutter level is calculated from the maximum measured RCS value in the absence of the test objects in the test environment. In order to ensure that only the relevant SPs are considered, a threshold is introduced, i.e., only RCS values of the VRUs or the human dummy that are at least 10 dB above the clutter level are considered in the evaluation. The signal processing chain for extracting the SP matrix of the object under test is shown in Fig. 7. It should be noted that RCS values are independent of the distance between the object and the sensor.

B. Extracted Radar Models

This section describes the measurement results of five different sized persons and a human dummy. The SPs and, consequently, the physical sizes of the persons under test can

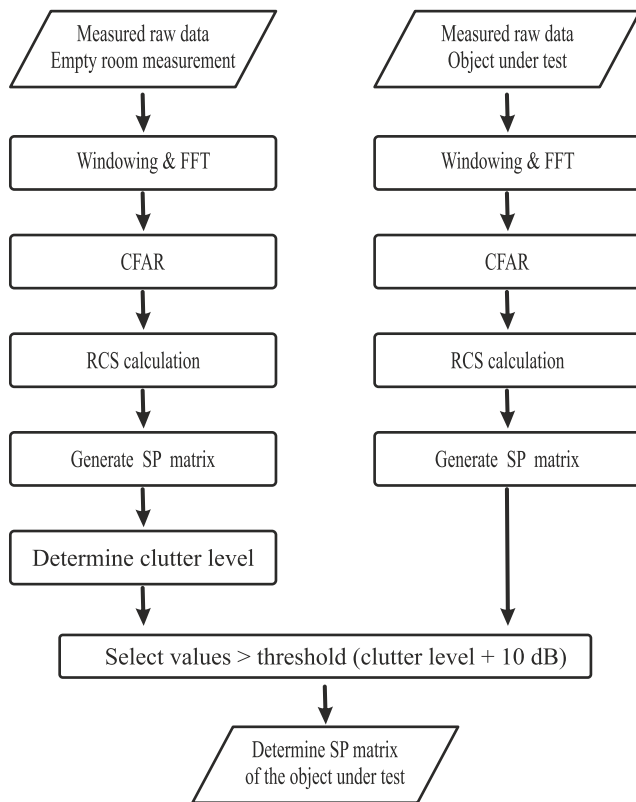


Fig. 7. Signal processing chain for extracting the SPs matrix from the high-resolution measurement data.

be derived from the measurement results. A high-resolution measurement is very challenging for the person under test since the person should not move during the measurement, which can extend to more than 2 h, depending on the resolution. The five test persons can be categorized by their sizes into skinny (A), small (B), kid-size (C), tall (D), and thickish (E). After that, a synthetic foam-based dummy is prepared with similar sizes to person (A). Since the physical dimension of person (A) and the dummy are nearly identical, similar results can be expected in the location of the main SPs as long as the model shows a similar reflection coefficient. Due to the short wavelength of the radar waves, the penetration depth into a body or material is very low [28]. For this reason, the main reflection is caused by the clothes of the person under test and the dummy. It is shown that absorption of mm-wave radar signals in the 76–81-GHz band in dry thin clothes is negligible [9]. However, these clothes may affect the positions of the peaks and nulls in the RCS patterns, especially when thicker clothing, weather, and bike protection clothing, or work clothing is used. Therefore, the test persons and dummy are dressed up with dry shirts and pants of thin cotton material. Test person (A) is measured with an increased resolution and the results are compared to the results of the dummy.

In order to determine the RCS characteristics of the persons under test and the dummy and to analyze the SPs of the object under test thoroughly, the radar models of these VRUs are computed. The extracted models provide the location of

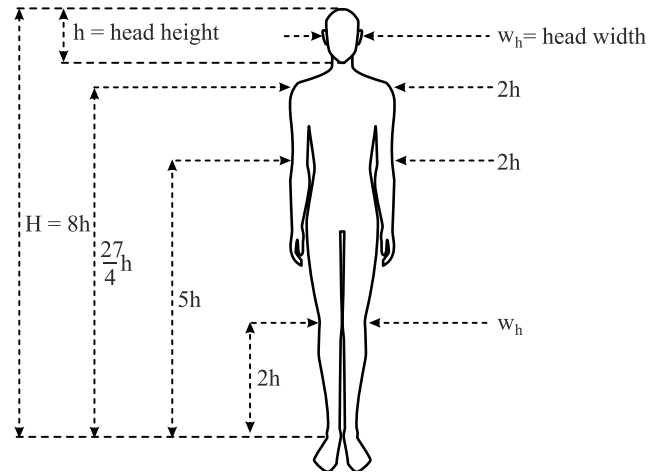


Fig. 8. Cardboard person model to show the details of each region of the human body with respect to the height of the head (h) and its width (w_h). The overall height of the human body (H) is eight heads. The expected height for the shoulders is $(27/4)h$ and the shoulder width is two times the head height. The elbows have a height of five heads and a width of two heads. The knees height is two times the head height and their width is equal to the width of the head (w_h).

the SPs over the body surface and their corresponding RCS values. The measurements are performed for persons (A)–(E) and dummy over the whole 360° azimuthal rotation angle with different step widths. Since the measurements require the persons to stand still in front of the sensor for a relatively long time (in average ~ 20 min for each azimuthal rotation angle), the measurements for persons (B)–(E) are performed with 90° step width. Nonetheless, these measurements are sufficient to detect certain parts of the body, as will be discussed later. In order to analyze the backscattering behavior of the dummy with respect to a real object of the same size [person (A)], these measurements are done with finer step widths. The measurements on the dummy are performed with steps of 10°. The rotation step size for person (A) is selected 30° in order to keep the measurement time at a tolerable level. It should be noted that all models are specified homogeneous since the electromagnetic waves at the working frequencies do not penetrate through the skin layer [28] and the clothing.

The Radar system in the test setup of Fig. 3 is scanning the elevation direction with steps of $\Delta\theta = 1^\circ$ to cover the whole height of the human body or dummy under test. The azimuth scanning range is assigned according to the width of the object under test and all the objects are scanned with $\Delta\phi = 1^\circ$. In this manner, the assigned scanning areas can cover the whole dimension of the targets.

Fig. 8 shows the four major human body parts, i.e., head, shoulder, elbow, and knee. These parts are the reference for analyzing the extracted models of the persons and dummy human under test. The measured data and plotted radar models for the persons under test (A)–(E) and the dummy are shown in Figs. 9 and 10, respectively. The rotation table moves clockwise and $\beta = 0^\circ$ is defined as the rotation angles where the object front is toward the sensor. $\phi = 0^\circ$ and $\theta = 0^\circ$ are aligned to the middle of the object under test. The clutter level of the test environment is -45 dBsm. Therefore, Figs. 9 and 10 are plotted for SPs with RCS values higher than -35 dBsm.

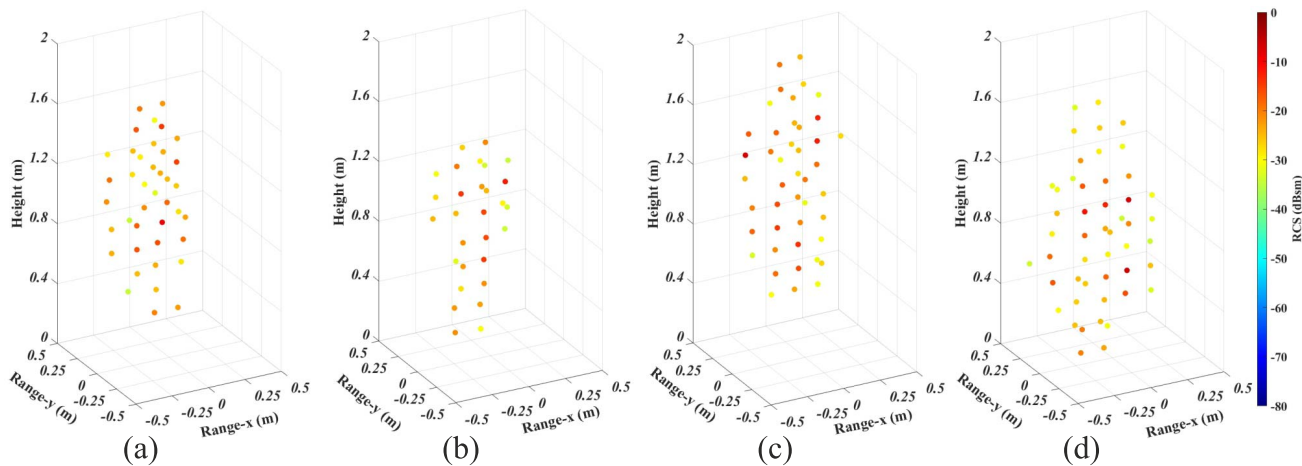


Fig. 9. Extracted radar model of the different size human bodies in front view ($\beta = 0^\circ$). The center of the persons corresponds to a range of 0 m. The starting rotation angle of the Radar system ($\phi = 0^\circ$ and $\theta = 0^\circ$) is toward the middle of the person under test. The points with RCS less than -35 dBsm are neglected. (a) Person (B). (b) Person (C). (c) Person (D). (d) Person (E).

Although different rotation angles of the person under test have been measured and investigated, for the sake of clarity, only the extracted radar models at the front side ($\beta = 0^\circ$) with the corresponding SPs of persons (A)–(E) are shown in detail in Figs. 9 and 10(a). The contour and the orientation of persons can be interpreted from Figs. 9 and 10(a).

For comparing the backscattering behavior of the human and the dummy, the extracted radar models of person (A) and the dummy in front view (stage rotation angle of $\beta = 0^\circ$) are shown in Fig. 10(a) and (c), respectively. The left side view ($\beta = 90^\circ$) is given in Fig. 10(b) and (d). The RCS values of the extracted scattering points in the **SP** matrix for the front view of the human vary within the range of -34.9 dBsm to -14.1 dBsm. These values for the dummy human in the same view are within the range of -34.1 dBsm to -14.5 dBsm. Considering the **SP** matrix of person (A) and its dummy in the side view, it can be realized that the RCS values are between -34.9 dBsm and -16.9 dBsm for human and between -34.0 dBsm and -14.4 dBsm for the dummy. The outline and the orientation of person (A) and dummy can be seen in Fig. 10(a)–(d).

For quantitative analysis, the derived sizes of the reconstructed models are compared with their actual sizes in the next step. Therefore, a dedicated algorithm is used to analyze the extracted positions of the SPs of different human parts. This algorithm is developed based on the cardboard model (human body proportions theory) [29], [30], which is the used model for human tracking in video sensor-based systems [31]. This model is based on the proportions of a human body. It specifies the relative positions and sizes of the body parts using the height of the head (h) with a high degree of accuracy. The model states that a person can be represented by a set of connected planar patches [29]. Fig. 8 shows the cardboard human model of an upright standing person. This model contains the height and position details of each region to determine their approximate location. As the first step, the height of the person under study (H) is extracted. According to the model, the overall height of the person under study (H) is eight times the head height (h) and the shoulders are

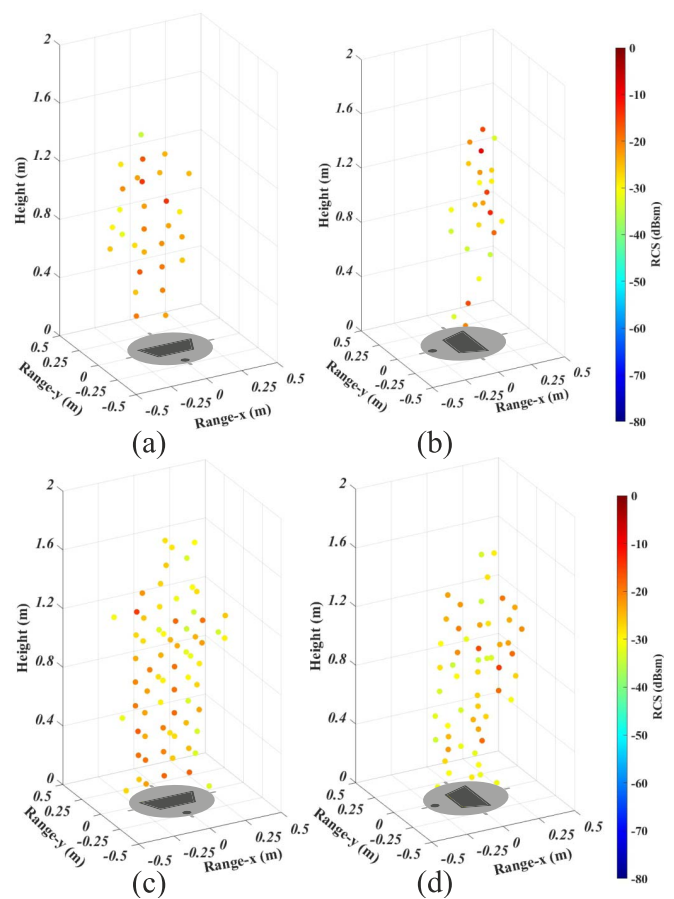


Fig. 10. Extracted radar model of person (A) and human dummy in front view ($\beta = 0^\circ$) and in left side view ($\beta = 90^\circ$). The center of the objects under test corresponds to a range of 0 m. The starting rotation angle of the Radar system ($\phi = 0^\circ$ and $\theta = 0^\circ$) is toward the middle of the person under test. The points with RCS less than -35 dBsm are neglected. (a) Person (A) with the stage rotation angle of 0° . (b) Person (A) with the stage rotation angle of 90° . (c) Human dummy with the stage rotation angle of 0° . (d) Human dummy with the stage rotation angle of 90° .

placed at the height of $(27/4)h$ heads and their width is $2h$. The elbows are located at the height of around five heads and their width is roughly the same as the shoulder width. Knees

TABLE II

COMPARISON OF THE ACTUAL AND MEASURED (IN PARENTHESIS) PHYSICAL DIMENSIONS AND THE CORRESPONDING RCS VALUES OF THREE BODY REGIONS OF DIFFERENT HUMAN OBJECTS AND DUMMY HUMAN FOR 76–81-GHz MONOSTATIC RCS DATA COLLECTION. RCS VALUES OF EACH REGION ARE THE SUM OF ALL RCS VALUES OF THE SPs WITHIN THAT DOMAIN

VRU model	Sizes (cm)							RCS (dBsm)		
	Height	Shoulder height	Shoulder width	Elbow height	Elbow width	Knee height	Knee width	Head	Torso	Legs
A	170 (163)	144 (148)	40 (32)	103 (116)	47 (47)	50 (53)	21 (16)	-15.8	-8.3	-8.2
B	173 (181)	147 (135)	44 (48)	112 (118)	50 (48)	54 (54)	20 (16)	-10.3	-4.8	-6
C	158 (156)	134 (124)	43 (47)	94 (108)	45 (48)	47 (45)	18 (16)	-16.1	-7	-9.8
D	192 (199)	165 (152)	47 (48)	126 (136)	52 (48)	57 (56)	30 (32)	-8.7	-2.6	-6.8
E	180 (177)	149 (145)	45 (48)	115 (130)	58 (48)	60 (66)	30 (32)	-12	-1.4	-3.8
Dummy human	170 (173)	136 (138)	42 (34)	111 (107)	48 (32)	52 (43)	21 (16)	-19.1	-7.6	-9.4

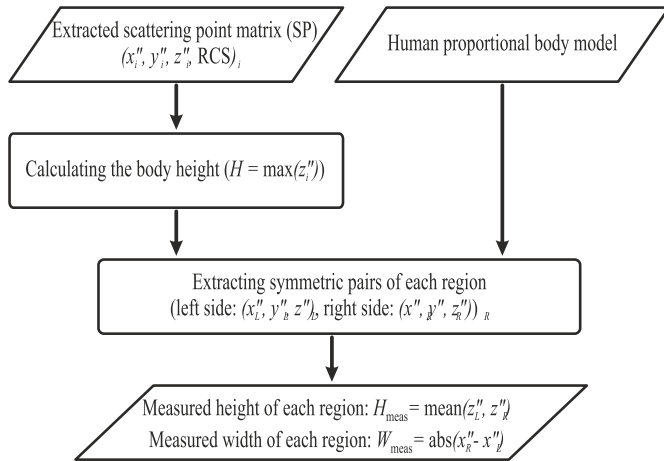


Fig. 11. Signal processing chain for extracting the measured size of different human region.

are located at the height of $2h$ with the width the same as the head width (w_h). The block diagram of the algorithm is shown in Fig. 11. The inputs of the algorithm are the extracted SPs matrix of the person under test (**SP**) and the human proportional body model. Then, the algorithm calculates the overall height of the human body (H). Subsequently, the algorithm searches for the relevant points of the body regions (knees, elbows, shoulders, and head) based on their expected heights. The width of each body region is specified by the coordinates of corresponding right and left sides $[(x''_R, y''_R, z''_R)]$ and (x''_L, y''_L, z''_L) , respectively].

After the determination of symmetric pairs of individual body parts, their height and width can be calculated. The height of each region is the average of the height of the region in right and left sides $[(\text{mean}(z''_R, z''_L))]$. The algorithm estimates the width of every region by

$$W_{\text{Meas}} = |x''_R - x''_L|. \quad (13)$$

Table II lists the actual physical sizes of the test persons and the human dummy and their measured sizes from the extracted radar models for the mentioned points in Fig. 8.

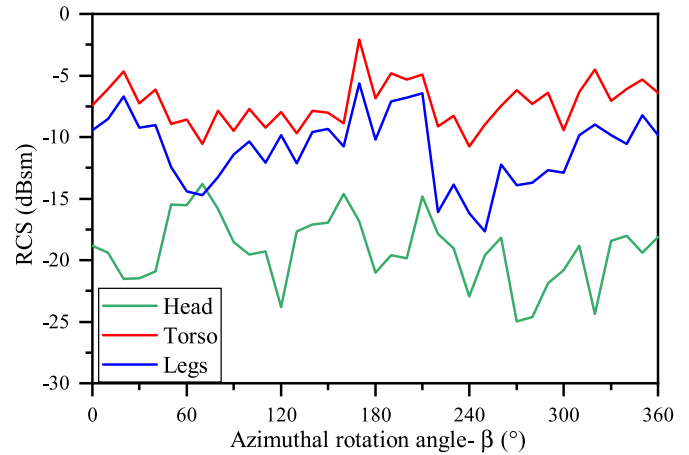


Fig. 12. Corresponding RCS values of three body regions (head, legs, and torso) of the dummy human in different azimuthal rotation angles (β). The values are the summation of different SPs within the corresponding region.

According to Table II, the differences between the extracted and the actual sizes of the body regions are smaller than 16 cm. Taking the HPBW of 1.3° for the Radar system, the expected illuminated area of the body under test is $20 \text{ cm} \times 20 \text{ cm}$ in the distance of 9 m from the Radar system. Therefore, the measurement error is attributed to the measurement resolutions and the measured values are in good agreement with actual sizes. Moreover, this comparison validates the accuracy of the measurements and postprocessing steps.

In the next step, the backscattering behavior of the test persons is analyzed quantitatively. For this purpose, the human body, shown in Fig. 8, is divided into three major regions: head (the range between $7h$ and $8h$), torso (the range between $4h$ and $7h$), and legs (the range between 0 and $4h$). The summation of the measured RCS values for the extracted SPs inside each region is introduced as the RCS value of the related region. These values can be found in Table II. The comparison between the RCS values of the different regions for every test person and the dummy shows that the torso

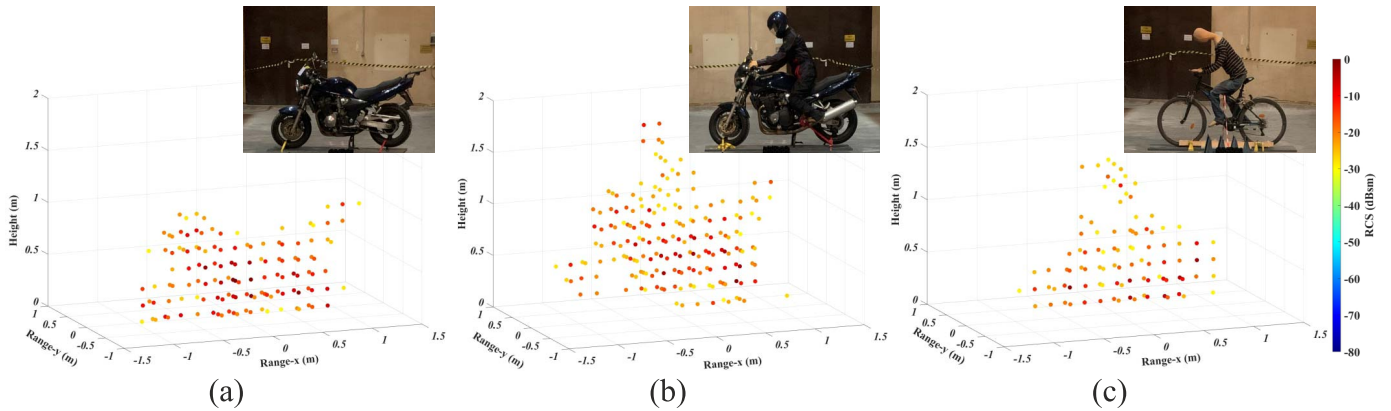


Fig. 13. Extracted radar model of (a) motorcycle, (b) motorcyclist, and (c) bicycle in side view ($\beta = 90^\circ$). The insets also show the photographs of the corresponding objects as the reference. The center of the objects under test corresponds to a range of 0 m. The starting rotation angle of the Radar system ($\phi = 0^\circ$ and $\theta = 0^\circ$) is toward the middle of the objects. The points with RCS less than -35 dBsm are neglected.

dominates their backscattering behavior. The next strongest scattering area in human body regions comes from the legs and the lowest influence in the backscattering behavior can be attributed to the head region. Fig. 12 shows the calculated RCS values for different body regions of the human dummy for different azimuthal rotation angles. As expected, this figure clearly illustrates that the strongest scatterings occur in back side and the weakest scatterings come from the side views. The given RCS values for different regions are in good agreement with the results presented in [9]. By comparing the RCS values corresponding to the same body region in different test persons, one can notice that larger body regions result in larger RCS values. As an example, the test person (E) has a larger torso compared to other test persons, and therefore, the RCS of its torso is the largest value. The smallest RCS values are related to the skinny (A) and kid-size (C) persons, as they have smaller body regions.

For a more detailed comparison between person (A) and dummy, the RCS values of the similar body regions of both objects under study are inspected. It is observed that each individual body part in the case of person (A) and dummy has similar RCS values with a maximum 2-dB difference. As an example, the extracted RCS value for the right elbow of the human and dummy are -20.0 dBsm and -21.0 dBsm, respectively. According to these results, the dummy under test has a similar backscattering behavior compared to person (A). This means that the dummy can be used for even higher resolved measurements where the measurement time exceeds several hours. This reduces measurement errors due to movements of the test persons. This conclusion confirms that the human can be replaced with the dummy in the measurement scenarios for VRUs. The measurements for the dummies with different sizes are available, and however, this is not discussed in this work.

Furthermore, the measurement technique is extended to other road users, e.g., motorcycles and bicycles. As discussed previously, the dummy human can be used as the cyclist or the motorcyclist. It makes it possible to measure a cyclist and motorcyclist over the whole 360° azimuthal rotation angle with 10° step width. The extracted SPs of the motorcycle with

and without its motorcyclist, and bicycle with its cyclist are presented in Fig. 13(a)–(c), respectively. Fig. 13 reveals the capability of this technique to differentiate between various VRUs. Accordingly, the extracted radar models can also be employed for target classification.

Figs. 9, 10, and 13 show that the profile of each object under test is recognizable through the distribution of the SPs. The employed Radar system in the measurement setup has the capability to extract the radar image of the object under test. As it is discussed in Section I, this feature helps in target classification, especially when the specific RCS contributions are considered together with micro-Doppler measurements. The extracted radar images can provide data in azimuth and elevation directions, and therefore, the shape and size of the object under test can be captured. Bearing in mind that different VRUs have distinct spans in the azimuth and elevation direction, different types of VRUs can be easily distinguished. For example, a pedestrian has a smaller extension in the azimuth direction and a larger extension in the elevation direction compared to a bicycle, motorcycle, or vehicle.

IV. CONCLUSION

In this article, a high-resolution measurement setup for the determination of the spatially distributed scattering centers of different VRUs is presented. The measurement setup is based on an mm-wave radar sensor with 5-GHz bandwidth around a center frequency of 79.5 GHz. In combination with a high focusing lens with an HPBW of 1.3° , high-resolution measurements in distance as well as in both azimuth and elevation angles are possible. With this measurement setup, different sized VRUs have been measured with a scanning resolution of the radar of 1° at different rotation angles of the VRUs. The test persons cover skinny, small, kid-sized, tall, and thickish persons and hence cover the variety of real-world road users. Since a complete 360° high-resolution RCS measurement of a VRU is very time-consuming and thus leads to errors due to unintended motion of the person under test, an additional measurement is performed using a human dummy instead of a real test person. It is shown that the relevant SPs can be clearly detected over the body surface.

A further investigation of the SPs showed that they match very well with the physical size of the test persons. The human dummy and the corresponding test person also show very similar values in the size and the distribution of the SPs allowing even higher resolved RCS data. Finally, relevant body parts can now be mapped to certain RCS values. This not only helps in the classification of the VRUs but also enables the development of realistic target models in wave propagation software and paves the way to develop VRU models that can assign micro-Doppler values with a verified RCS value to the different extremities of a human body. The results of this article can also be used in SiL, HiL, or OTA/ViL setups for the evaluation of ADAS functions for future AD.

In a further step, it is also possible to assign the extracted RCS values to specific micro-Doppler values of the extremities, but this is not part of this work.

ACKNOWLEDGMENT

The authors would like to thank Prof. G. Müller from the Institute for Pulsed Power and Microwave Technology (IHM), Karlsruhe Institute of Technology (KIT), Karlsruhe, Germany, for providing the test environment.

REFERENCES

- [1] N. K. Ragesh and R. Rajesh, "Pedestrian detection in automotive safety: Understanding state-of-the-art," *IEEE Access*, vol. 7, pp. 47864–47890, 2019.
- [2] S. M. Patole, M. Torlak, D. Wang, and M. Ali, "Automotive radars: A review of signal processing techniques," *IEEE Signal Process. Mag.*, vol. 34, no. 2, pp. 22–35, Mar. 2017.
- [3] R. Perez, F. Schubert, R. Raschofer, and E. Biebl, "Single-frame vulnerable road users classification with a 77 GHz FMCW radar sensor and a convolutional neural network," in *Proc. 19th Int. Radar Symp. (IRS)*, Jun. 2018, pp. 1–10.
- [4] Y. Chen, S. Chen, T. Xiao, S. Zhang, Q. Hou, and N. Zheng, "Mixed test environment-based vehicle-in-the-loop validation—A new testing approach for autonomous vehicles," in *Proc. IEEE Intell. Vehicles Symp. (IV)*, Oct. 2020, pp. 1283–1289.
- [5] M. Maurer, J. C. Gerdes, B. Lenz, and H. Winner, *Autonomes Fahren: Technische, Rechtliche und Gesellschaftliche Aspekte*. Wiesbaden, Germany: Springer, May 2015, doi: 10.1007/978-3-662-45854-9.
- [6] P. Koopman and M. Wagner, "Challenges in autonomous vehicle testing and validation," *SAE Int. J. Transp. Saf.*, vol. 4, no. 1, pp. 15–24, Apr. 2016.
- [7] A. Diewald *et al.*, "Radar target simulation for vehicle-in-the-loop testing," *Vehicles*, vol. 3, no. 2, pp. 257–271, May 2021.
- [8] S. Abadpour, A. Diewald, B. Nuss, M. Pauli, and T. Zwick, "Extraction of scattering centers using a greedy algorithm for traffic participants," in *Proc. 14th Eur. Conf. Antennas Propag. (EuCAP)*, Mar. 2020, pp. 1–5.
- [9] M. Chen and C.-C. Chen, "RCS patterns of pedestrians at 76–77 GHz," *IEEE Antennas Propag. Mag.*, vol. 56, no. 4, pp. 252–263, Aug. 2014.
- [10] T. Schipper, J. Fortuny-Guasch, D. Tarchi, L. Reichardt, and T. Zwick, "RCS measurement results for automotive related objects at 23–27 GHz," in *Proc. IEEE 5th Eur. Conf. Antennas Propag. (EuCAP)*, Apr. 2011, pp. 683–686.
- [11] H. Buddendick and T. F. Eibert, "Incoherent scattering-center representations and parameterizations for automobiles," *IEEE Antennas Propag. Mag.*, vol. 54, no. 1, pp. 140–148, Feb. 2012.
- [12] H. Buddendick and T. F. Eibert, "Acceleration of ray-based radar cross section predictions using monostatic-bistatic equivalence," *IEEE Trans. Antennas Propag.*, vol. 58, no. 2, pp. 531–539, Feb. 2010.
- [13] K. Schuler, D. Becker, and W. Wiesbeck, "Extraction of virtual scattering centers of vehicles by ray-tracing simulations," *IEEE Trans. Antennas Propag.*, vol. 56, no. 11, pp. 3543–3551, Nov. 2008.
- [14] S. Abadpour, A. Diewald, M. Pauli, and T. Zwick, "Extraction of scattering centers using a 77 GHz FMCW radar," in *Proc. 12th German Microw. Conf. (GeMic)*, Mar. 2019, pp. 79–82.
- [15] S. Abadpour, A. Diewald, S. Marahrens, M. Pauli, and T. Zwick, "Back scattering of traffic participants based on an automotive radar measurement," in *Proc. 17th Eur. Radar Conf. (EuRAD)*, Jan. 2021, pp. 99–102.
- [16] X. Cai, M. Giallorenzo, and K. Sarabandi, "Machine learning-based target classification for MMW radar in autonomous driving," *IEEE Trans. Intell. Vehicles*, vol. 6, no. 4, pp. 678–689, Dec. 2021.
- [17] O. Schumann, M. Hahn, J. Dickmann, and C. Wohler, "Semantic segmentation on radar point clouds," in *Proc. 21st Int. Conf. Inf. Fusion (FUSION)*, Jul. 2018, pp. 2179–2186.
- [18] S. Lee, Y.-J. Yoon, J.-E. Lee, and S.-C. Kim, "Human-vehicle classification using feature-based SVM in 77-GHz automotive FMCW radar," *IET Radar, Sonar Navigat.*, vol. 11, no. 10, pp. 1589–1596, Aug. 2017.
- [19] M. Goldhammer, S. Köhler, S. Zernetsch, K. Doll, B. Sick, and K. Dietmayer, "Intentions of vulnerable road users—Detection and forecasting by means of machine learning," *IEEE Trans. Intell. Transp. Syst.*, vol. 21, no. 7, pp. 3035–3045, Jul. 2020.
- [20] D. Belgiovan, C.-C. Chen, M. Chen, S. Y.-P. Chien, and R. Sheron, "77 GHz radar scattering properties of pedestrians," in *Proc. IEEE Radar Conf.*, May 2014, pp. 735–738.
- [21] N. Yamada, Y. Tanaka, and K. Nishikawa, "Radar cross section for pedestrian in 76 GHz band," in *Proc. Eur. Microw. Conf. (EuMC)*, Oct. 2005, p. 1018.
- [22] E. Schubert, M. Kunert, W. Menzel, J. Fortuny-Guasch, and J. Chareau, "Human RCS measurements and dummy requirements for the assessment of radar based active pedestrian safety systems," in *Proc. 14th Int. Radar Symp. (IRS)*, Jun. 2013, pp. 752–757.
- [23] N. Pohl, T. Jaeschke, S. Kueppers, C. Bredendiek, and D. Nüßler, "A compact ultra-wideband mmWave radar sensor at 80 GHz based on a SiGe transceiver chip (focused session on highly-integrated millimeter-wave radar sensors in SiGe BiCMOS technologies)," in *Proc. Int. Microw. Radar Conf. (MIKON)*, May 2018, pp. 345–347.
- [24] L. Piotrowsky, T. Jaeschke, S. Kueppers, J. Siska, and N. Pohl, "Enabling high accuracy distance measurements with FMCW radar sensors," *IEEE Trans. Microw. Theory Techn.*, vol. 67, no. 12, pp. 5360–5371, Dec. 2019.
- [25] M. Pieraccini, L. Miccinesi, and N. Rojhani, "RCS measurements and ISAR images of small UAVs," *IEEE Aerosp. Electron. Syst. Mag.*, vol. 32, no. 9, pp. 28–32, Sep. 2017.
- [26] C. A. Balanis, *Antenna Theory: Analysis and Design*, 3rd ed. New York, NY, USA: Wiley, Jan. 2005.
- [27] M. A. Richards, J. A. Scheer, and W. A. Holm, *Principles of Modern Radar: Basic Principles*. Rijeka, Croatia: SciTech, 2010.
- [28] M. Chen, M. Kuloglu, and C.-C. Chen, "Numerical study of pedestrian RCS at 76–77 GHz," in *Proc. IEEE Antennas Propag. Soc. Int. Symp. (APSURSI)*, Jul. 2013, pp. 1982–1983.
- [29] S. X. Ju, M. J. Black, and Y. Yacoub, "Cardboard people: A parameterized model of articulated image motion," in *Proc. IEEE 2nd Int. Conf. Autom. Face Gesture Recognit.*, Oct. 1996, pp. 38–44.
- [30] I. Haritaoglu, D. Harwood, and L. Davis, "W⁴: Who? When? Where? What? A real time system for detecting and tracking people," in *Proc. IEEE 3rd Int. Conf. Autom. Face Gesture Recognit.*, Apr. 1998, pp. 222–227.
- [31] K. Sato, B. L. Evans, and J. K. Aggarwal, "Designing an embedded video processing camera using a 16-bit microprocessor for a surveillance system," *J. VLSI Signal Process.*, vol. 42, no. 1, pp. 57–68, Jan. 2006.



Sevda Abadpour (Member, IEEE) received the B.Sc. degree in electrical engineering and information technology from the Iran University of Science and Technology (IUST), Tehran, Iran, in 2008, and the M.Sc. degree in electrical engineering and information technology from the Amirkabir University of Technology (AUT), Tehran, in 2011. She is currently pursuing the Ph.D. degree in electrical engineering at the Institute of Radio Frequency Engineering and Electronics (IHE), Karlsruhe Institute of Technology (KIT), Karlsruhe, Germany.

Her current research interests include automotive radar channel modeling and electromagnetic wave propagation. The focus of her work is radar cross section (RCS) measurement for traffic participants and the development of radar models for the use in over-the-air (OTA) vehicle-in-the-loop (ViL) test method.



Sören Marahrens received the B.Sc. (B.S.E.E.) and M.Sc. (M.S.E.E.) degrees in electrical engineering and information technology from the Karlsruhe Institute of Technology (KIT), Karlsruhe, Germany, in 2013 and 2016, respectively.

From 2016 to 2021, he worked as a Research and Teaching Assistant at the Institute of Radio Frequency Engineering and Electronics (IHE), KIT. Since 2021, he has been working as an EMC and Radio Test Engineer at Nemko GmbH & Co. KG, Pfinztal, Germany. His main fields of research

interest include millimeter-wave antennas, including lens antenna systems, millimeter-wave packaging, and digital signal processing for radar systems.



Mario Pauli (Senior Member, IEEE) received the Dipl.Ing. (M.S.E.E.) degree in electrical engineering from the University of Karlsruhe, Karlsruhe, Germany, in 2003, and the Dr.Ing. (Ph.D.E.E.) degree from the Karlsruhe Institute of Technology (KIT), Karlsruhe, in 2011.

In 2002, he spent four months at the IBM T. J. Watson Research Center, Yorktown Heights, NY, USA, working on time- and frequency-domain measurement systems for the characterization of the 60-GHz indoor radio channel. From 2004 to 2011,

he was with the Institut für Höchstfrequenztechnik und Elektronik (IHE), University of Karlsruhe, as a Research Assistant. Since 2011, he has been with the Institute of Radio Frequency Engineering and Electronics (IHE), KIT, as a Senior Researcher and a Permanent Lecturer. He served as a Lecturer for radar and smart antennas of the Carl Cranz Series for Scientific Education. He is currently a Co-Founder and the Managing Director of PKTEC GmbH, Karlsruhe, and a Co-Founder of Wellenzahl Radar- und Sensortechnik GmbH & Company KG, Karlsruhe. His current research interests include radar and sensor systems, radar cross section (RCS) measurements, antennas, wave propagation, and millimeter-wave packaging.



Jan Siska (Member, IEEE) received the B.Sc. and M.Sc. degrees in electrical and information engineering from Ruhr University Bochum, Bochum, Germany, in 2015 and 2018, respectively, where he is currently pursuing the Ph.D. degree at the Institute of Integrated Systems.

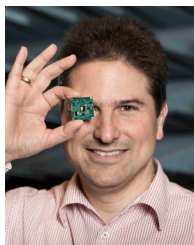
His main research interests include digital signal processing, millimeter-wave radar system design, and vital sign detection using frequency-modulated continuous-wave (FMCW) radar sensors.



Nils Pohl (Senior Member, IEEE) received the Dipl.Ing. and Dr.Ing. degrees in electrical engineering from Ruhr University Bochum, Bochum, Germany, in 2005 and 2010, respectively.

From 2006 to 2011, he was a Research Assistant with Ruhr University Bochum, where he was involved in integrated circuits for millimeter-wave (mm-wave) radar applications. In 2011, he became an Assistant Professor with Ruhr University Bochum. In 2013, he became the Head of the Department of mm-Wave Radar and High Frequency Sensors, Fraunhofer FHR, Wachtberg, Germany. In 2016, he became a Full Professor of integrated systems with Ruhr University Bochum. In parallel, he is the Head of the Research Group for Integrated Radar Sensors, Fraunhofer FHR. He has authored or coauthored more than 200 scientific articles and has issued several patents. His current research interests include ultrawideband mm-wave radar, design, and optimization of mm-wave integrated SiGe circuits and system concepts with frequencies up to 300 GHz and above, as well as frequency synthesis and antennas.

Dr. Pohl was a co-recipient of the 2009 IEEECom Innovation Award, the Best Paper Award at EUMIC 2012, the Best Demo Award at RWW 2015, and the Best Student Paper Awards at RadarConf 2020 and RWW 2021. He was a recipient of the Karl-Arnold Award of the North Rhine-Westphalian Academy of Sciences, Humanities and the Arts in 2013 and the IEEE MTT Outstanding Young Engineer Award in 2018.



Thomas Zwick (Fellow, IEEE) received the Dipl.Ing. (M.S.E.E.) and Dr.Ing. (Ph.D.E.E.) degrees from the Universität Karlsruhe, Karlsruhe, Germany, in 1994 and 1999, respectively.

From 1994 to 2001 he was a Research Assistant at the Institut für Höchstfrequenztechnik und Elektronik (IHE), Universität Karlsruhe. In February 2001, he joined the IBM T. J. Watson Research Center, IBM, Yorktown Heights, NY, USA, as a Research Staff Member. From October 2004 to September 2007, he was with Siemens AG, Lindau,

Germany. During this period, he managed the RF development team for automotive radars. In October 2007, he became a Full Professor at the Karlsruhe Institute of Technology (KIT), Karlsruhe. He is also the Director of the Institute of Radio Frequency Engineering and Electronics (IHE), KIT. He is the coeditor of three books and the author or coauthor of 120 journal articles and over 400 contributions at international conferences. He holds 15 granted patents. His research topics include wave propagation, stochastic channel modeling, channel measurement techniques, material measurements, microwave techniques, millimeter-wave antenna design, wireless communication, and radar system design.

Dr. Zwick has been a member of acatech (German National Academy of Science and Engineering) since 2019. Since 2017, he has been a member of the Heidelberg Academy of Sciences and Humanities. His research team received over ten best paper awards at international conferences. He served on the technical program committee (TPC) of several scientific conferences. He was the General Chair of the International Workshop on Antenna Technology (iWAT 2013), Karlsruhe, in 2013, and the IEEE MTT-S International Conference on Microwaves for Intelligent Mobility (ICMIM), Heidelberg, in 2015. He was the TPC Chair of the European Microwave Conference (EuMC) in 2013 and the General TPC Chair of the European Microwave Week (EuMW) in 2017. In 2023, he will be the General Chair of EuMW, Berlin. From 2008 until 2015, he was the President of the Institute for Microwaves and Antennas (IMA). He was selected as a Distinguished IEEE Microwave Lecturer for the term of 2013–2015 with his lecture on “QFN Based Packaging Concepts for Millimeter-Wave Transceivers.” In 2019, he was the Editor-in-Chief of the IEEE MICROWAVE AND WIRELESS COMPONENTS LETTERS.